CORA Cork Open Research Archive
Cartlann Taighde Oscailte Chorcaí

Title	Dual-functionality of NiSe2-CoSe2 nanowires for electrochemical charge storage and efficient thermal energy conversion
Authors	Palanisamy, Rupa Ranjani;Padmanathan, N.;Ashokan, Anjali;Tanwar, Amit;Biswas, Subhajit;Holmes, Justin D.;Razeeb, Kafil M.
Publication date	2025
Original Citation	Palanisamy, R. R., Padmanathan, N., Ashokan, A., Tanwar, A., Biswas, S., Holmes, J. D. and Razeeb, K. M. (2025) 'Dual-functionality of NiSe2-CoSe2 nanowires for electrochemical charge storage and efficient thermal energy conversion', Journal of Energy Storage, 121, p.116568. DOI: 10.1016/j.est.2025.116568
Type of publication	Article (peer reviewed)
Link to publisher's version	10.1016/j.est.2025.116568
Rights	© 2025, the Author(s). . Published by Elsevier Ltd. This is an open access article under the CC BY license (http://creativecommons.org/licenses/by/4.0/) - https://creativecommons.org/licenses/by/4.0/
Download date	2026-11-07 13:19:13
Item downloaded from	https://hdl.handle.net/10468/17323



University College Cork, Ireland
Coláiste na hOllscoile Corcaigh

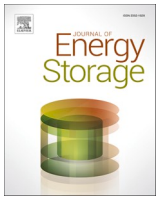
Journal of Energy Storage 121 (2025) 116568



Contents lists available at ScienceDirect

Journal of Energy Storage

journal homepage: www.elsevier.com/locate/est



Research papers



Dual-functionality of $NiSe_2$-$CoSe_2$ nanowires for electrochemical charge storage and efficient thermal energy conversion

Rupa Ranjani Palanisamy [a,b,c], N. Padmanathan [a], Anjali Ashokan [b], Amit Tanwar [a], Subhajit Biswas [b,c], Justin D. Holmes [b,c], Kafil M. Razeeb [a,*]

[a] Micro-Nano System Centre, Tyndall National Institute, Cork T12 R5CP, Ireland
[b] School of Chemistry, University College Cork, Cork T12 YN60, Ireland
[c] Environmental Research Institute, University College Cork, Cork T23 XE10, Ireland

ARTICLE INFO

Keywords:
Energy storage
Electrode fabrication
$NiSe_2$-$CoSe_2$ nanowires
Thermo-electrochemical cell
Thermal energy harvesting

ABSTRACT

Thermo-electrochemical cell coupled with an electrochemical energy storage device creates a comprehensive harvesting system that can convert thermal energy into electrical energy and store it. Thus, the development of electrodes that demonstrate high efficiencies in electrochemical and thermoelectric properties is crucial, as they serve as the fundamental components in energy conversion and storage systems. This study presents the synthesis of $NiSe_2$-$CoSe_2$ (NCS) nanowires on activated carbon cloth (ACC) substrate, for enhanced electrochemical charge storage and ionic-thermoelectric applications. Comparative analysis demonstrates that NCS/ACC electrodes significantly outperform monometallic selenides in both electrochemical performance and thermoelectric applications. The NCS/ACC electrode revealed a maximum charge storage capacity of 112 mA hg^{-1} at a current density of 1 A g^{-1}. Utilizing 1 M NaOH as an aqueous electrolyte, the NCS/ACC system showcases its pioneering role in thermo-electrochemical cell (TEC), opening avenues for efficient heat-to-electricity conversion. The NCS/ACC-based TEC delivered a Seebeck coefficient of −3.4 mV K^{-1} and thermal charge storage of −1.02 J. These findings reveal the dual functionality of nickel cobalt selenides, offering promising solutions for thermal energy harvesting and storage in electrochemical systems.

1. Introduction

The escalating demand for advanced energy storage and conversion technologies has spurred significant interest in transition metal selenides (TMSs) electrodes [1–3]. TMSs demonstrate a diverse array of oxidation states and superior electronic conductivity (10^{-3} S m^{-1}) when compared to metal oxides (1×10^{-5} S m^{-1}) and sulphides (5×10^{-28} S m^{-1}) [4]. In contrast, alternative materials such as carbon, conductive polymers, transition metal oxides, and hydroxides exhibit limitations in terms of their low capacitance, self-degradation, and inadequate rate capability and conductivity [5]. The bimetallic selenides deliver superior electrochemical charge storage performance when compared to single metals due to their lower band gap energy and higher redox activity [5]. Among TMSs, Ni—Co selenides have grabbed recent research attention owing to their remarkable electrochemical performance [6,7]. The redox properties of Ni—Co selenides are promisingly higher because of the synergistic effect derived from nickel and cobalt. For instance, NiCoSe nanosheets @graphene [8], NiCoSe nanowires [9], NiCoSe nanorod [10], $NiCoSe_2$ nanoarrays [11] and CoNiSe @polypyrrole [12] based electrodes showed high electrochemical charge storage performance compared to that of the corresponding NiSe and CoSe electrodes [13]. Despite their promising electrochemical performance, Ni—Co selenides deliver elevated energy and power densities but often suffer from compromised cyclic stability and decreased capacity retention or vice-versa. Stability is frequently a critical challenge in redox electrodes, mainly arising from electrode material degradation associated with continuous insertion and extraction of charge carriers. This prolonged cycling process can induce physical deformations and delamination within the electrode matrix, ultimately compromising the structural integrity and electrochemical performance of the material. To tackle these limitations, it is essential to directly fabricate Ni—Co selenides on highly porous and conductive substrates like carbon cloth (CC). CC, with its high conductivity, large surface area, and flexibility, serves as an ideal substrate for binder-free electrodes, enabling efficient ion transport and enhancing overall electrochemical charge storage performance [14].

* Corresponding author.
E-mail address: kafil.mahmood@tyndall.ie (K.M. Razeeb).

https://doi.org/10.1016/j.est.2025.116568
Received 12 December 2024; Received in revised form 26 March 2025; Accepted 4 April 2025
Available online 14 April 2025
2352-152X/© 2025 The Author(s). Published by Elsevier Ltd. This is an open access article under the CC BY license (http://creativecommons.org/licenses/by/4.0/).

Integration of Ni—Co selenides with a CC substrate forms a hybrid electrode that synergistically combines the strengths of each component, enabling improved capacity retention, enhanced stability, and significant energy density. For instance, Ling et al. reported the high energy density (30.71 Wh kg^{-1}) and superior capacity retention (87.64 % for 2000 cycles) of CC coupled with $NiCo_2Se_4$ for an asymmetric supercapacitor (ASC) device [14]. However, the stability of Ni—Co selenides can be further maximized through strategies such as tailoring the morphology and optimizing the material composition to enhance electrochemical performance. Thereby, in this study, we fabricated $NiSe_2$-$CoSe_2$ (NCS) nanowires on activated carbon cloth (ACC) substrate as an advanced electrode for electrochemical charge storage applications. Comparative experiments with monometallic selenides ($NiSe_2$ and $CoSe_2$) demonstrate superior charge storage capacity of 112 mA hg^{-1} at a current density of 1 A g^{-1} for NCS-ACC electrode. NCS/ACC has simultaneously achieved enhanced cyclic stability (85 % capacity retention for 10,000 cycles) and high specific energy (28 Wh kg^{-1}), attributed to the combined effects of $NiSe_2$-$CoSe_2$ nanowires coupled with ACC.

While the electrochemical properties of Ni—Co selenides have been the focus of extensive research for electrochemical charge storage applications, another promising area that merits attention is the ionic thermoelectric or thermo-electrochemical cell. Traditional Thermoelectric generators (TEGs) have been widely investigated due to their capability of power generation from thermal energy. TEGs are based on semiconductor materials that produce thermoelectric voltage through the movement of charge carriers, such as electrons or holes, in response to a thermal gradient. TEGs are limited due to low Seebeck coefficient (few hundred microvolts per Kelvin) and the presence of toxic materials (e.g. Pb, Te, etc.), restricting their widespread use in harvesting low-grade heat energy [15]. This has redirected research focus towards ionic thermoelectric or thermoelectrochemical cell (TEC), which generates voltage due to thermodiffusion of ions and thermogalvanic effects at the electrode electrolyte interface under a thermal gradient [16]. A TEC can generate large ionic thermopower due to large ionic Seebeck coefficient, which is a hundred times larger than the electronic counterpart and can reach several mV K^{-1}.

TEC feature a simple design comprising metal (Pt, Au, Ni, Cu and Zn) [17,18] or carbon-based electrodes [17] encasing a redox couple electrolyte (e.g. $[Fe(CN)_6]^{4-}/[Fe(CN)_6]^{3-}$ or I^-/I_3^-) [19] and can generate potential differences in the order of 1–10 mV K^{-1} [16]. Redox electrolytes are used for TEC as they facilitate efficient charge transport through the reversible oxidation-reduction reactions, enabling substantial ion mobility in response to thermal gradients. This ionic conduction significantly enhances the electrochemical potential, ultimately improving the thermoelectric performance and ionic Seebeck coefficient of the TEC. For example, Kang et al. incorporated carbon electrodes in a redox couple electrolyte ($[Fe(CN)_6]^{4-}/[Fe(CN)_6]^{3-}$) based thermocell that resulted in a Seebeck coefficient of 1.43 mV K^{-1} [20]. Similarly, Kim et al. employed platinum electrodes in redox couple electrolyte ($[Fe(CN)_6]^{4-}/[Fe(CN)_6]^{3-}$), which produced a Seebeck coefficient of −1.29 mV K^{-1} [21]. Despite the promising potential of redox electrolytes, they produce highly toxic hydrogen gas under heating or acidic conditions. Also, in contrast to traditional noble metals and carbon-based materials, transition metal compounds (e.g. transition metal selenides) exhibit variable valences that facilitate dual redox reactions occurring in the electrolyte and the electrode. TMSs can offer unique advantages for enhancing the performance of TEC due to their favourable electrochemical properties and redox activity [4]. The high electrical conductivity of TMSs enables improved charge transfer kinetics, which is essential for optimizing the efficiency of thermo-voltage generation in TEC. For instance, Xinrui et al. fabricated a mixed-phase redox electrode ($MoSe_2$/NiSe on Ni foam) in 0.4 M $[Fe(CN)_6]^{4-}/[Fe(CN)_6]^{3-}$ electrolyte for TEC for a charge storage capacity of 222 mA h g^{-1} at 4 A g^{-1} and a Seebeck coefficient of −1.69 mV K^{-1} for low-grade heat harvesting (ΔT = 50 K) [22]. Although the $MoSe_2$/NiSe mixed-phase redox electrode demonstrates a significant ability to store charge, it delivered a low Seebeck coefficient, which indicates poor heat conversion efficiency. Therefore, modifications to the electrode's composition or structure are necessary to enhance the Seebeck coefficient and improve heat conversion efficiency.

The current work pioneers the application of NCS/ACC electrodes in TEC utilizing 1 M NaOH aqueous electrolyte, instead of traditional redox couples, which has not been reported before. NCS/ACC electrodes deliver a Seebeck coefficient of −3.4 mV K^{-1} and a thermal charge storage −1.02 J for a thermal gradient of 10 K. In this work, the NCS/ACC electrodes exhibit dual functionality by serving as an efficient electrochemical charge storage material and a promising candidate for thermal energy conversion. Their exceptional electrochemical performance enables high charge storage capacity and enhanced cyclic stability, making them suitable in advanced charge storage applications. Simultaneously, the incorporation of NCS/ACC in TEC achieved the effective conversion of heat to electricity. This dual functionality positions NCS/ACC as a potential candidate that not only enhances charge storage systems but also contributes in efficient heat energy harvesting, leading to innovative solutions in advanced energy technology.

2. Materials and methods

2.1. Chemicals

The chemicals were of analytical grade purity and used without further purification. Nickel Chloride hexahydrate ($NiCl_2{\cdot}6H_2O$), Cobalt chloride hexahydrate ($CoCl_2.6H_2O$), selenium dioxide (SeO_2), ammonium hydroxide (NH_4OH), and hydrazine hydrate ($N_2H_4.H_2O$, 98%pure) were purchased from Sigma–Aldrich (Ireland). Commercial plain carbon cloth – 1071 HCB with the thickness of 0.34 mm, pore density of 0.31 g m^{-3}, surface area of 1000 m^2 g^{-1}, and electrical conductivity of 106 S m^{-1} was purchased from Fuel cell store, USA.

2.2. Surface modification of CC

The carbon cloth's hydrophobic properties are attributed to its strong carbon-carbon bonding, hindering metal adhesion. Activation of the CC breaks these bonds, enabling metal deposition and promoting a strong surface bond formation [23]. A piece of acid treated (1:1 ratio of HNO_3 and H_2SO_4) CC with the dimension of 4 × 4 cm^2 was immersed into a 40 mL mixed solution containing KOH and ethanol solution (the weight ratio of KOH to CC is 1:4). Then the solution was continuously stirred for 3 h at a temperature of 80 °C to vaporise the solvent ethanol completely. Furthermore, the KOH-treated CC was annealed at a high temperature of 800 °C for 3 h with a temperature-ramping rate of 10 °C min^{-1}. Finally, the CC was washed with 2 M HCl followed by DI water for 1 h and dried at 60 °C overnight to obtain the activated carbon cloth (ACC). The contact angle measurement in Fig. S1 exhibits a significant shift from hydrophobic to hydrophilic properties of CC before and after KOH treatment. Following activation, the ACC surface displays enhanced hydrophilicity, facilitating improved adhesion of metal composites on the surface compared to the hydrophobic CC. The schematic representation of ACC preparation is given in Fig. S1 in the Supplementary information (SI).

2.3. Material preparation

The synthesis of $NiSe_2/CoSe_2$ nanowires on ACC (NCS/ACC) was achieved by facile one-pot hydrothermal synthesis. Typically, 0.05 M of $NiCl_2{\cdot}6H_2O$ (1 g), 0.05 M of $CoCl_2{\cdot}6H_2O$ (1 g) and 0.1 M SeO_2 (0.9 g) were added to 80 mL of deionized water, followed by stirring. Then 10 mL of $N_2H_4.H_2O$ and 12 mL of NH_4OH were slowly added dropwise to the homogeneous solution, while stirring for 30 min. The solution was transferred to a 100 mL Teflon-lined autoclave, and the ACC was completely immersed inside. The reaction vessel was sealed and placed

in an oven at 180 °C for 12 h. After the reaction, the autoclave was allowed to naturally cool down to room temperature. ACC was taken out of the autoclave and washed several times with acetone and deionized water. ACC was dried at room temperature and then annealed at 400 °C for 3 h to obtain the final product of $NiSe_2/CoSe_2$ nanowires on ACC (NCS/ACC). The synthesis of $CoSe_2$ on ACC (CS/ACC) and $NiSe_2$ on ACC (NS/ACC) follows an identical procedure, with a 1:1 M ratio of Ni to Co. The schematic diagram illustrating the overall process of electrode preparation is presented in Fig. S2. The details of material characterization, electrochemical and thermo-electrochemical measurements are given in the SI.

3. Results and discussions

3.1. Morphological and compositional analysis

Fig. 1(a and b), (d and e), and (g and h) shows the SEM images of NS/ACC, CS/ACC, and NCS/ACC respectively, with modulated morphologies such as microspheres, interconnected nanosheets, and nanowires, which are uniformly grown on carbon fibres. Fig. 1(a and b) shows that after the hydrothermal reaction, the $NiSe_2$ microspheres are uniformly grown on the ACC. The $NiSe_2$ microspheres exhibits a well-ordered array structure that fully cover the fibres of ACC. The microspheres form a network with plenty of pores and uneven spaces with a size distribution between 0.5 and 3 μm. Fig. 1(d and e) shows the well-established texture structure of the $CoSe_2$ nanosheets grown on the carbon fibres. Fig. 1(g and h) reveals the $NiSe_2$-$CoSe_2$ nanowire array architecture uniformly covering the skeletons of carbon fibre.

The grown nanowires mimic the densely packed bristles of a woolly caterpillar and are oriented almost vertically on the carbon fibre. The low magnification SEM images in Fig. S3 demonstrate the consistent and uniform growth of the active materials across all carbon fibres of the carbon cloth. The EDX spectra (Fig. S4) and elemental mapping in Fig. 1 (c, f and i) represent the chemical composition and atomic distribution in the as-prepared samples. The EDX analysis presented in Fig. S4(a–c) quantifies the atomic weight distribution percentages of Ni, Co, Se, and Carbon (C) in NS/ACC, CS/ACC, and NCS/ACC. Notably, the ACC substrate yields a high carbon content across all the samples. In the sample NS/ACC, the atomic weight percentages of Ni and Se were determined to be 5 % and 10 %, respectively. In CS/ACC, the atomic weight percentages of Co and Se were found to be 6.6 % and 13.3 %, respectively. Additionally, in the NCS/ACC sample, the atomic weight percentages of Ni, Co and Se were quantified as 13.01 %, 16.6 %, and 25.08 %, respectively. Notably, it was observed that the concentration of selenium is approximately twice that of both nickel and cobalt in all the samples. No other impurity signal was present in the sample. This observation supports the presence $NiSe_2$, $CoSe_2$, and phases of mixed $NiSe_2$-$CoSe_2$ within the samples. These findings affirm the purity and

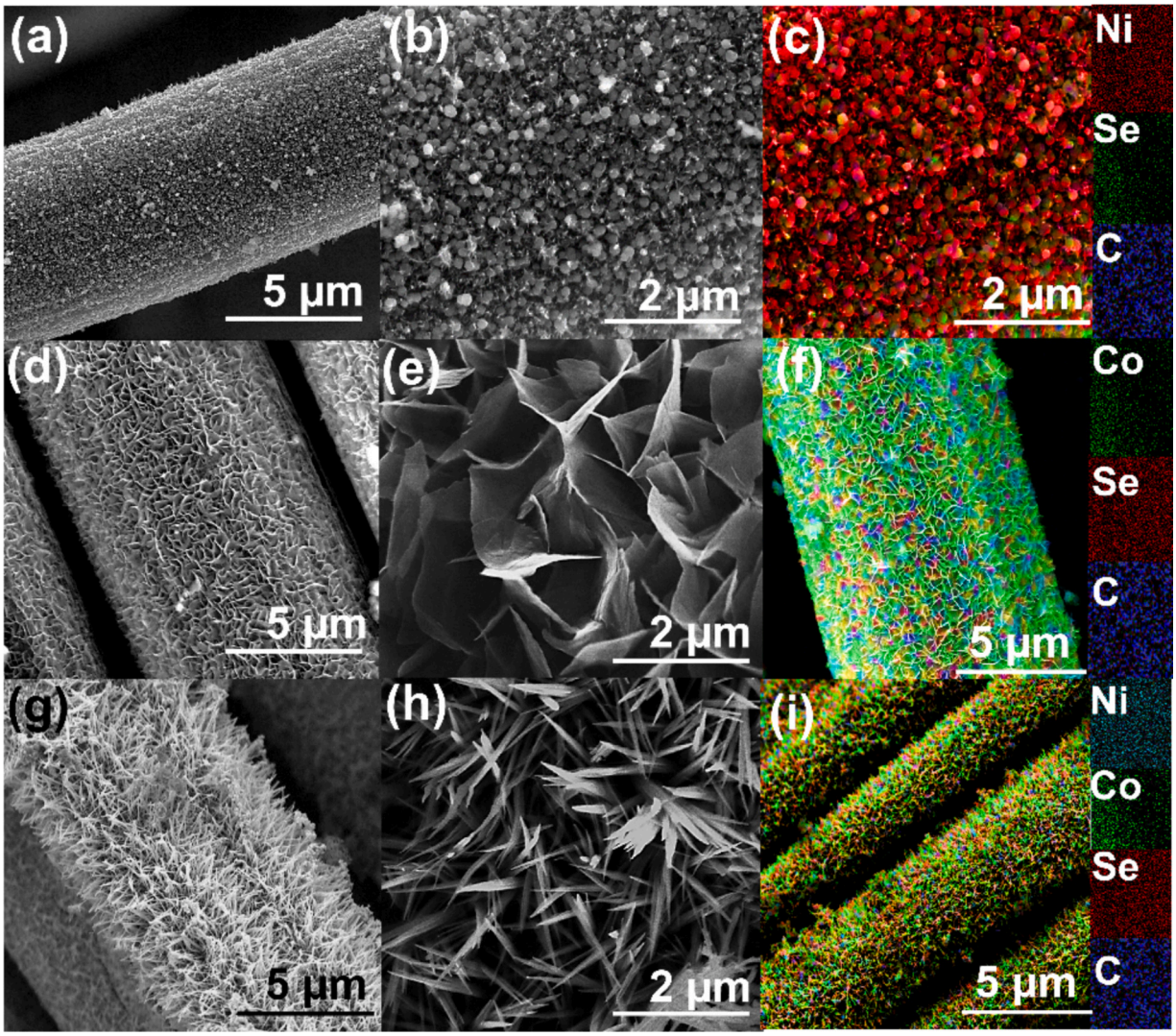


Fig. 1. SEM images and elemental mapping of (a–c) NS/ACC, (d–f) CS/ACC and (g–i) NCS/ACC hydrothermally synthesized at 180 °C for 12 h.

composition of elements within the NS/ACC, CS/ACC, and NCS/ACC composites.

The TEM analysis in Fig. S5 confirms the crystalline properties and microstructure of the selenide electrodes through high-resolution transmission electron microscopy (HRTEM) and selected-area electron diffraction (SAED) patterns. The low magnification TEM images in Fig. S5(a–c) and corresponding inset images of NS/ACC, CS/ACC, and NCS/ACC clearly show the formation of spheres, interconnected nanosheets, and nanowires, respectively. Fig. S5(d–f) shows the HRTEM images of the selenide electrodes, wherein the d-spacings of 0.293, 0.285 and 0.24 nm are observed, corresponding to the (200) plane of $NiSe_2$, (101) plane of $CoSe_2$ and (211) plane of $NiSe_2$-$CoSe_2$ respectively. Also, the SAED patterns (Fig. S5(g and h)) clearly show the (211) and (210) planes of $NiSe_2$ and (110), and (101) planes of $CoSe_2$. Fig. S5(i) exhibits nanocrystalline characteristics with well-ordered diffraction rings, which are indexed to (101) and (211) planes of $NiSe_2$-$CoSe_2$ [24–27]. The SEM and TEM analysis reveal that the $NiSe_2$-$CoSe_2$ nanowires on ACC are grown vertically with the average length of about 3 μm and a tip diameter of ~11 nm.

Fig. 2(a) shows the XRD analysis of all the selenide samples. The broad diffraction peak at 25° and 44° in all three patterns can be indexed to the (002) and (101) planes, which indicates the crystalline phase of the ACC substrate [28]. The XRD graph for NS/ACC indicates the peaks at 30°, 33.83°, 37°, 51.2°,55.8°, 58° and 64.5° related to (200), (210), (211), (311), (023), (321) and (400) planes of the cubic phase of $NiSe_2$ (JCPDS card no. 53-0449) [28]. Likewise, the XRD spectrum of the CS/ACC indexed at angles 30.5°, 34.2°, 35.9° and 63.2° are associated to planes (110), (011), (101), and (122), which shows the formation of orthorhombic phase of $CoSe_2$ (JCPDS card no. 88-1711) [29].

The sample NCS/ACC exhibit characteristic peaks at 29.8°, 33.4°, 36.9°, 37.9°, 51° and 55.5° which are assigned to the (200), (210), (211), (220), (311) and (023) planes of $NiSe_2$ and the peaks at 57° and 63.6° are assigned to (131) and (122) planes of $CoSe_2$ [28–30]. The sample NCS/ACC exhibits similar patterns to $NiSe_2$ and $CoSe_2$, confirming the formation of $NiSe_2$ and $CoSe_2$ on ACC. Raman analysis (Fig. 2(b)) further confirmed the existence of graphitized carbon with obvious D band and G band vibrations of carbon peaks located at 1356 and 1590 cm^{-1}, respectively [31]. The Raman peaks of NS/ACC located at 151, 170, 215 and 233 cm^{-1} are attributed to the T_g, E_g, A_g and T_g modes of $NiSe_2$ cubic phase and are in good agreement with the previously reported values [32,33]. Three peaks at 177, 521 and 685 cm^{-1} in the Raman spectra of CS/ACC correspond to the Se—Se stretching mode of $CoSe_2$ [29,30,34]. Furthermore, the peaks of NCS/ACC are located at 231 cm^{-1} and 177 cm^{-1}, which is the simple superposition of $NiSe_2$ and $CoSe_2$ [35–37].

Fig. 3(a) shows the XPS survey spectra of NS/ACC, CS/ACC and NCS/ACC, which exhibit the signals of Ni, Se, Co, O, and C elements. The C element results from the ACC substrate (Fig. S7(a)), and O may originate from the atmospheric moisture or slight oxidation of the electrode surface [38]. Notably, the XPS signal of Ni 2p appeared while that of Co 2p was absent in NS/ACC, conversely absence of Ni 2p and the presence of Co 2p are visible in CS/ACC, as shown in Fig. 3(b and c). Both the Co 2p and Ni 2p XPS signals are observed in the NCS/ACC sample. The high-resolution XPS spectra of C1s in all the prepared samples are shown in Fig. S7(a). And the high-resolution Ni 2p, Co 2p and Se 3 s XPS peaks of the samples are shown in Fig. 3(b–d). In the Ni spectrum, the peaks at 853.7 eV and 855.7 eV (in the Ni $2p_{3/2}$ band) are attributed to Ni^{2+}. The satellite peaks at 861.2 and 864.4 eV can also be ascribed to Ni $^{2+}$ [39,40]. The peak at 780.1 eV (in the Co $2p_{3/2}$ band) is attributed to Co^{3+}, and the satellite peaks at 782.3, 785.9 and 788.1 eV (in the Co $2p_{3/2}$ band) are also observed for Co^{3+} [41,42]. The peak at 230 eV corresponds to Se 3 s and 233 eV, which is likely related to SeO_2 as shown in Fig. S7(b) [9,43]. The Fig. 3(d) shows Se 3d XPS spectra for all three samples, where the broad peak at 59 eV can be due to selenium–oxygen bonding structure, which comes from the surface oxidation state of Se species [44]. Meanwhile, the peak at 54.6 eV belongs to Se $3d_{5/2}$, which confirms the selenium–metal bonding [42,45]. The XPS analysis has confirmed the presence of nickel-cobalt selenides in the NCS/ACC material, indicating their coexistence within the sample.

3.2. Electrochemical charge storage

All the synthesized electrodes (CS/ACC, NS/ACC, NCS/ACC) including ACC were subjected to a comparative cyclic voltammetry (CV) analysis at a scan rate of 5 mV s^{-1} within the potential range of 0–0.45 V, as shown in Fig. 4(a). Among all the CV profiles, NCS/ACC exhibited a relatively superior electrochemical performance with a high current and large integral area, indicating greater specific capacity of NCS/ACC than its single counterparts. The superior electrochemical performance of NCS/ACC in comparison to NS/ACC and CS/ACC can be attributed to its synergistic effect arising from the combined properties of both Ni and Co. This bimetallic selenide promotes the number of active sites available for redox reactions, resulting in improved electrochemical activity. Further, the nanowire-like morphology provides a large surface area and shortens the pathways for OH^- ions and electron transport during the charge storage and release processes [46]. Fig. 4 (b–d) shows the CVs of all three electrodes at different scan rates ranging from 5 to 50 mV s^{-1}. The CV curve of CS/ACC (Fig. 4(b)) shows two small pairs of reversible redox peaks due to $Co^{2+/3+}$ and $Co^{3+/4+}$, which is due to Faradaic redox behaviour [47]. The proposed reaction mechanism of CS/ACC electrodes in the alkaline electrolyte is given below [48,49],

$$CoSe_2 + H_2O + \frac{1}{2}O_2 \rightarrow Co(OH)_2 + 2Se, \quad (1)$$

$$Co(OH)_2 + OH^- \leftrightarrow CoOOH + H_2O + e^-, \quad (2)$$

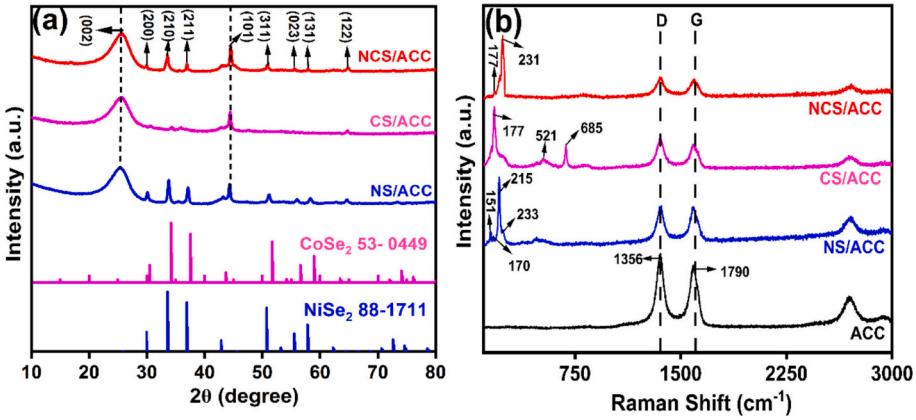


Fig. 2. (a) XRD and (b) Raman analysis of NS/ACC, CS/ACC, and NCS/ACC, respectively.

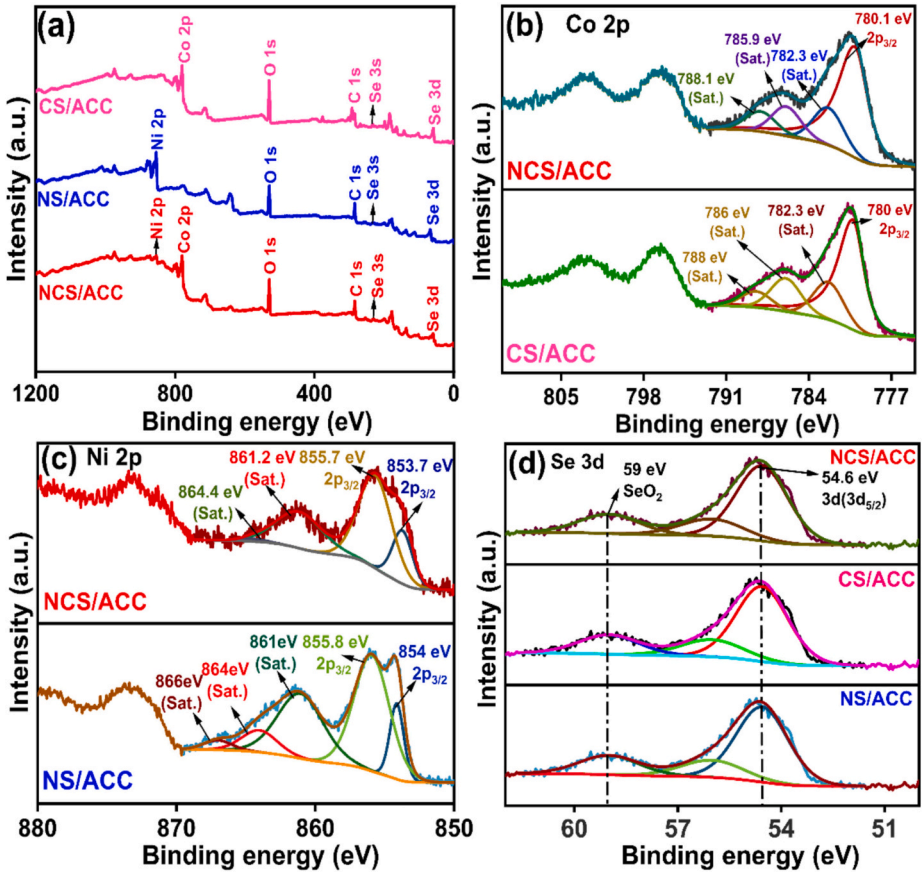


Fig. 3. (a) XPS survey spectrum and high-resolution XPS spectra of CS/ACC, NS/ACC and NCS/ACC, (b) Ni 2p, (c) Co 2p, and (d) Se 3d.

$$CoOOH + OH^- \leftrightarrow CoO_2 + H_2O + e^-, \quad (3)$$

Similarly, the possible reaction mechanism of NS/ACC electrode with OH^- ions is given below [48,49].

$$NiSe_2 + H_2O + \frac{1}{2}O_2 \rightarrow Ni(OH)_2 + 2Se, \quad (4)$$

$$Ni(OH)_2 + OH^- \leftrightarrow NiOOH + H_2O + e^-, \quad (5)$$

Fig. 4(c and d) shows that the electrodes NS/ACC and NCS/ACC exhibited prominent oxidation and reduction peaks in their respective cyclic voltammetry (CV) curves, indicating their battery-type behaviour. Also, it shows the typical Faradaic redox reaction of nickel and cobalt-containing alkaline electrolytes.

As shown in Fig. 4(d), the redox peaks of NCS/ACC electrode shift towards positive or negative potential with an increase in scan rate, indicating a diffusion-controlled mechanism. Also, the oxidation peaks of NCS/ACC electrode have a positive shift at higher scan rates because the rapid diffusion of ions is hindered at the innermost active sites of the electrode. Only at a lower scan rate (Fig. S8), the diffusion of ions from the electrolyte enters almost all the effective pores of the electrode [48,49]. In Fig. 4(e, f) the current density of all the electrodes is plotted against the square root of scan rate. All the electrodes exhibited a linear relationship, which confirms diffusion-controlled Faradaic process in the charge storage mechanism in selenide electrodes.

Two distinct mechanisms, such as surface and diffusion-controlled process, govern the total electrochemical charge storage process. The surface-controlled mechanism is a capacitive process, which entails the electrochemical adsorption and desorption of ions at the interface of the electrode and electrolyte (capacitive behaviour), as well as surface Faradaic redox reactions (pseudocapacitive behaviour) [50]. Whereas the diffusion-controlled process involves cation intercalation within the electrode material and ion diffusion within the electrolyte, which is often referred to as the battery-type mechanism [51]. The following equation gives a relationship between the current generated in the electrodes and the steady scan rate, which effectively classifies the contributions of these mechanisms [52],

$$i = av^b \quad (6)$$

where i is the current (mA), v is the scan rate (mV s^{-1}), and a and b are constants.

The value of b is equal to 0.5 and 1 in case of diffusion and surface-controlled process, respectively [53]. Fig. S9 shows the slopes (related to b value) of all the fabricated selenide electrodes, and the calculated b value of NCS/ACC is 0.58. This number is close to 0.5 and strengthens the claim of a reversible battery-type charge storage mechanism. The contributions of capacitive behaviour (k_1v) and diffusion behaviour ($k_2v^{1/2}$) can be estimated by analysing the current response obtained from the cyclic voltammetry (CV) curve at a designated voltage. This relationship can be expressed mathematically using the following equation [54]:

$$i(V) = k_1v + k_2v^{1/2} \quad (7)$$

where I is the measured current (mA) at a constant applied potential (V), v is the ramping scan rate (mV s^{-1}), and k_1 and k_2 denote the capacitive and diffusion-controlled effects [55,56]. Fig. S10(a) shows the percentage of diffusion and capacitive contribution and S10(b) shows the contributions of two different charge storage mechanisms in the CV curve at a 10 mV s^{-1} scan rate. Hence, it can be confirmed that the NCS/ACC is primarily governed by battery-type characteristics or a diffusion-controlled mechanism.

Further, GCD analysis was carried out to examine the

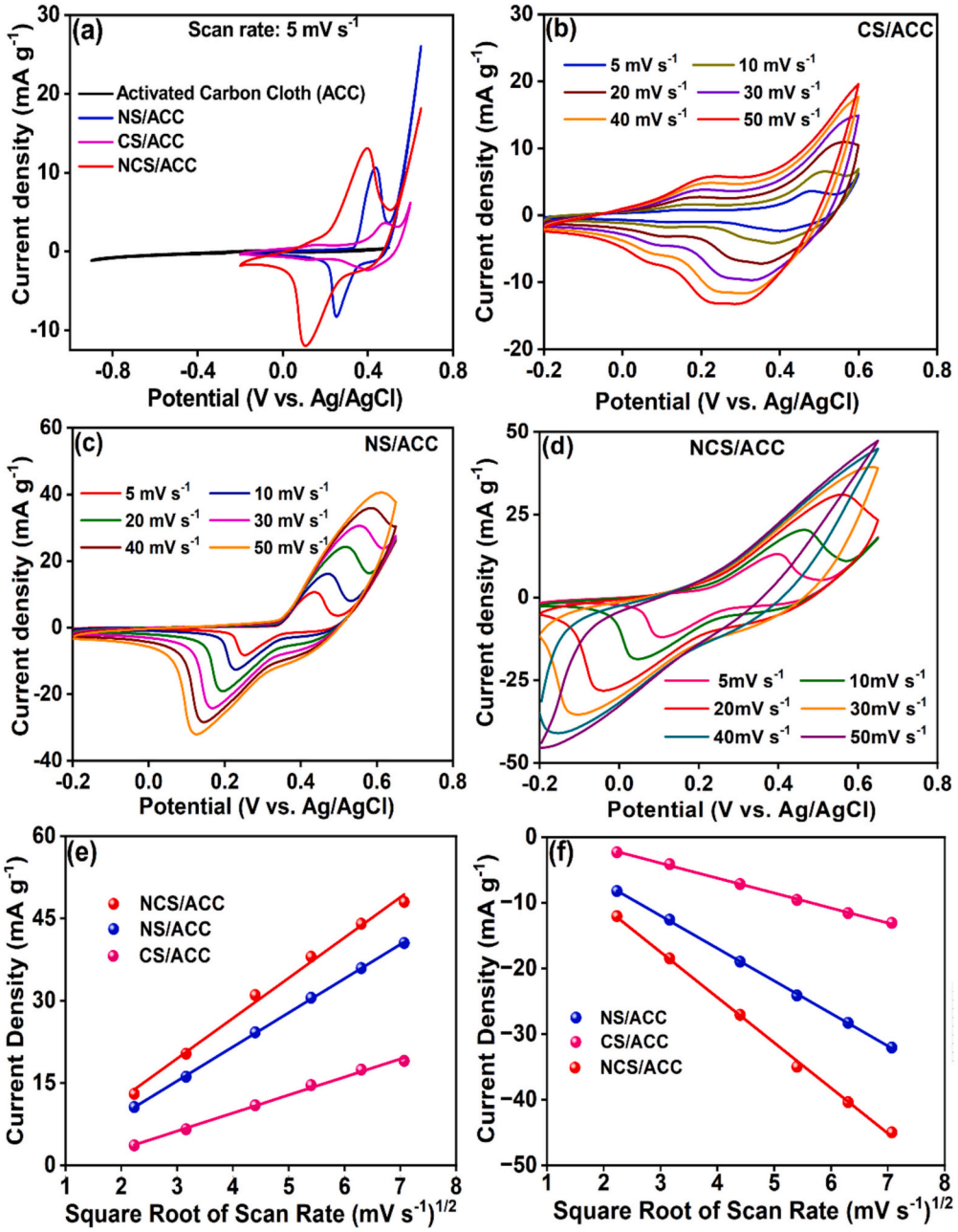


Fig. 4. (a) Comparative CV plots of all the electrodes at a scan rate of 5 mVs^{-1}. CV curves of the (b) CS/ACC, (c) NS/ACC, and (d) NCS/ACC at various scan rates from 5 to 50 mV s^{-1}. Relationship between (e) anodic and (f) cathodic peak currents as a function of square root of scan rate. In all cases, the R^2 linear fit is close to 0.99.

electrochemical charge storage performance of the prepared selenide electrodes, followed by the specific capacity calculation using Eq. (8). Fig. 5(a) shows the GCD curves of the electrodes at a current density of 1 A g^{-1} in the potential range of 0–0.45 V. Fig. 5(c–d) depicts GCD curves of NS/ACC and NCS/ACC electrodes have clear charge-discharge plateaus that correspond to the redox peaks observed in the CV curves. These plateaus are caused by the interaction between the OH^- ions in the electrolyte and the electrode material [44]. Fig. 5(b) shows the GCD curve of CS/ACC, which did not show typical Faradaic behaviour [44,57]. As shown in Fig. 5(d) NCS/ACC electrode has the longest discharging time at a current density of 1 mA g^{-1}, indicating the strongest charge storage characteristic.

In a three-electrode system, the specific charge storage capacity (mAh g^{-1}) can be calculated by the following Eq. (8) [58,59]:

$$C_s = \frac{I \times t}{3.6 \times m} \tag{8}$$

where I denote the discharge current (mA), t is the discharge time (s), and m is the mass of the active material (mg).

Similarly, the specific capacitance (F g^{-1}) in the three-electrode system can be determined using Eq. (9):

$$C_s = \frac{I \times t}{m \times V} \tag{9}$$

where I is the current (mA), t is the discharge time (s), m is the mass loading of active material (mg), and V is the cell voltage. The NCS/ACC electrode shows a charge storage capacity of 112 mAh g^{-1} (893 F g^{-1}) at a current density of 1 A g^{-1}, which decreases to 89 mAh g^{-1} (713 F g^{-1}) at a current density of 10 A g^{-1}. The NCS/ACC electrode shows superior

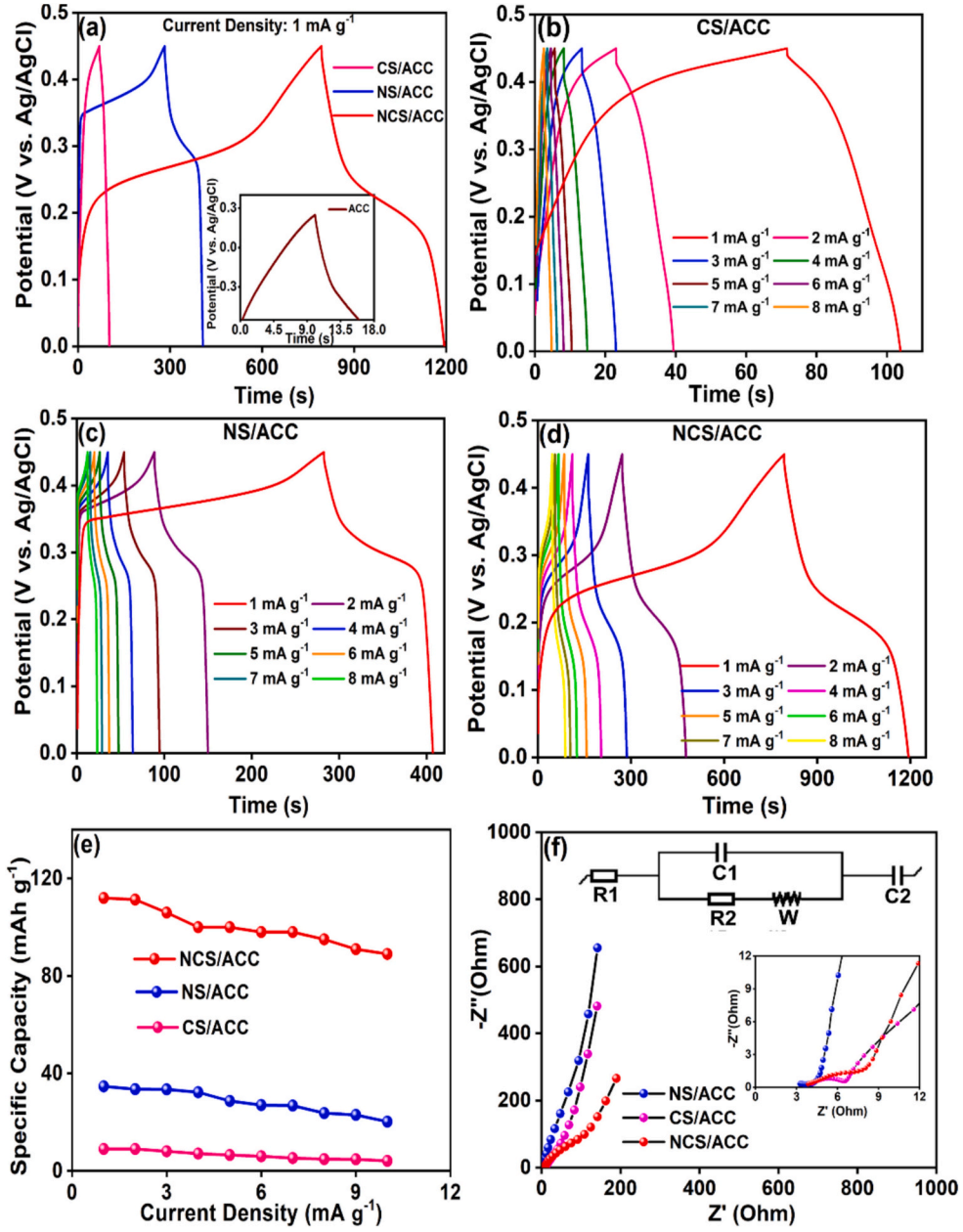


Fig. 5. (a) Comparative GCD profile CS/ACC, NS/ACC and NCS/ACC electrodes at 1 mA g^{-1}. GCD profile of the (b) CS/ACC, (c) NS/ACC and (d) NCS/ACC at various current densities from 1 to 8 mA g^{-1}. (e) Comparing the specific capacities of the electrodes at various current densities. (f) Comparative Nyquist plots of all the electrodes at a frequency range of 5 mHz to 70 kHz.

electrochemical performance compared to CS/ACC (73 F g^{-1} at 1 A g^{-1}) and NS/ACC (277 F g^{-1} at 1 A g^{-1}) electrodes. The enhanced electrochemical activity of NCS/ACC seems to originate from the combined redox reaction of $NiSe_2$ and $CoSe_2$, in addition to the nanowire morphology that attributes many active sites for the intercalation of OH^- ions on the electrode surface [27,60]. Fig. 5(e) shows the comparison of specific capacities as a function of the current densities of all the selenide electrodes. CS/ACC and NS/ACC electrodes showed a rapid decrease in the specific capacity for the increased current density and resulted in lower rate capability retention of 44 % and 58 %, respectively. Single metal selenides typically exhibit limited electronic conductivity and restricted ionic diffusion pathways due to lower charge carrier mobilities. This limits their electrochemical performance, particularly in charge storage applications, as efficient charge transport is essential for high-capacity and high-rate capabilities. The synergistic electrochemical performance of Ni and Co in NCS/ACC results in enhanced charge storage capability due to the complementary effects of the two metals. Ni contributes to increased high specific capacitance, while Co enhances structural stability and facilitates ion transport. This combination allows for improved electrochemical performance in energy storage applications, which is evident from Figs. 4(a) and 5(a). Hence, NCS/ACC benefits from a bimetallic structure and revealed significantly a higher specific capacity at 1 A g^{-1} and higher rate capability retention (79 %). This confirms the importance of NCS/ACC composite electrodes in achieving the synergistic enhancement of charge storage performance.

EIS analysis was carried out to evaluate the conductivity behaviour and charge transfer kinetics of the electrodes. The Nyquist plots shown in Fig. 5(f) exhibit semi-circular arcs in the high-frequency region and a linear tail in the low-frequency region for all the electrodes. The x-intercept in the high-frequency region corresponds to the total solution resistance (R_s) of the cells, which includes the ohmic resistance of the

electrolyte, the electronic resistance of the active materials, and the contact resistance between the electrode and the current collector [61]. The diameter of the semi-circular arc gives the charge transfer resistance (R_{ct}). The inset within Fig. 5(f) presents the equivalent circuit model consisting of R_s (R1), R_{ct} (R2), specific capacitance resulting from double layer formation (C1) and Faradaic redox reaction (C2), along with the Warburg impedance (W) utilized for estimating the diffusion of ions towards the electroactive surface [62]. The R_s values of NS/ACC, CS/ACC and NCS ACC are 3.2, 3.7 and 3.8 Ω, respectively. The R_{ct} values for the NS/ACC, CS/ACC and NCS/ACC electrodes are 0.34, 2.1 and 3.6 Ω, respectively. The R_{ct} value for the NCS/ACC electrode is slightly elevated compared to both the NS/ACC and CS/ACC electrodes. This increase in charge transfer resistance can be attributed to the multiphase coexistence of $NiSe_2$ and $CoSe_2$, which introduces additional interface barriers. These barriers arise from disparities in electronic properties and interfacial interactions between the distinct phases, consequently resulting in heightened resistance to charge transfer processes. This finding aligns with previous studies by Xia et al. and Zheng et al., who reported R_{ct} values of 9.46 Ω and 20.1 Ω, respectively, for $NiSe_2/CoSe_2$ electrodes [63,64]. Also, the R_{ct} value obtained for our NCS/ACC electrodes is significantly improved (3.6 Ω), indicating enhanced charge transfer characteristics compared to the recently reported values [63,64]. Although the R_s value of the NCS/ACC electrode is close to that of the other two selenium electrodes, the lower transfer resistance may be related to the dense nanowire structure. The overall outcomes of the EIS showcase the enhanced electrical conductivity and proficient charge transfer by the NS/ACC, CS/ACC and NCS/ACC electrodes.

The capacity retention of CS/ACC, NS/ACC and NCS/ACC are 83 %, 50 % and 98 %, respectively, for 600 charge-discharge cycles, as shown in Fig. S11. It is obvious that NCS/ACC retained the initial specific capacity after 600 cycles and surpassed the stability of CS/ACC and NS/ACC. NCS/ACC shows superiority over the other electrodes not only in terms of electrochemical charge storage performance but also in the aspect of rate capability.

Due to its superior electrochemical performance, the NCS/ACC electrode was used to develop an asymmetric supercapacitor (ASC). Activated carbon (AC) and NCS/ACC were used as the negative and positive electrodes, respectively. The ASC was assembled in the PAT-core cell with 100 µl of 1 M NaOH electrolyte with a celgard separator between NCS/ACC (anode) and activated carbon (cathode). Fig. S12(a) shows the CV curves of ACC and NCS/ACC with potential windows of −0.8 to 0.4 and −0.2 to 0.65 at 10 mV s^{-1}, respectively. Fig. S12(b) shows the CV curves of the assembled ASC at various scan rates, which exhibit hybrid capacitor behaviour due to synergistic contributions of the electric double layer (EDL) of the activated carbon and redox reaction of NCS/ACC [60]. The GCD curves at various current densities from 1 to 10 A g^{-1} are shown in Fig. S12(c). The maximum specific capacity calculated from the GCD curve is 34 mAh g^{-1} (75 F g^{-1}) at a current density of 1 A g^{-1} (Fig. S13). The Nyquist plot obtained from EIS in Fig. S12(d) reveals low R_s and R_{ct} values of 1.08 Ω and 14.92 Ω, respectively, which lead to the excellent electrochemical performance of NSC/ACC//AC ASC.

Fig. S14(a) represents the cycling performance of the assembled ASC where the device exhibits an excellent capacity retention of 85 % even after 10,000 stable charge-discharge cycles at a low current density of 2.5 A g^{-1}. The distinctive mesoporous one-dimensional structure and large surface area of the NCS/ACC nanowires offer a shortened diffusion path for the transport of electrons and ions between the electrode and electrolyte interface, thereby enhancing redox kinetics. As illustrated in Fig. S14(a), there is an initial loss of capacitance attributed to the multiphase nature of the $NiSe_2$ and $CoSe_2$ components. Nevertheless, once the structure stabilizes, it enhances the rate capability, leading to more efficient charge storage in subsequent cycles [63,64]. Overall, the NSC/ACC//AC ASC exhibits an excellent electrochemical performance and shows significant reversibility and stability.

The specific energy (S_E) and specific power (S_P) of the ASC can be calculated using the following equations [65,66],

$$S_E = \frac{C_s \times V^2}{2 \times 3.6}\ Wh\ kg^{-1} \tag{10}$$

$$S_P = \frac{S_E \times 3600}{\Delta t}\ W\ kg^{-1} \tag{11}$$

Fig. S14(b) shows the Ragone plot, which compares the specific energy as a function of the specific power of our NCS/ACC//AC-based ASC with previously reported devices. The NCS/ACC//AC ASC yields a S_E of 28 Wh kg^{-1} at a S_P of 646 W kg^{-1}, which is comparatively higher than the previously reported ASC devices based on Ni and Co selenides, as shown in Table S1. Compared to other NiSe and CoSe-based ASC, NCS/ACC//AC ASC also exhibit excellent cyclic stability (85 % capacity retention after 10,000 cycles), confirming improved electrochemical charge storage performance.

3.3. Thermoelectrochemical cell

3.3.1. Isothermal characterization

To explore the roles of redox reactions and ion diffusion in the ionic thermoelectric process, a series of temperature coefficient measurements was performed using a three-electrode setup. These temperature coefficient (TC) measurements were carried out across a temperature range from 25 to 60 °C, employing a three-electrode isothermal characterization method. This method helps to understand the change in single electrode potential resulting from a uniform temperature increase [67]. Fig. S15 shows the open circuit voltage (OCV) as a function of temperature for different systems. In each system, working and counter electrodes are identical (selenide electrodes), the reference Ag/AgCl was employed, and the electrolyte was 1 M NaOH. All the systems show decreasing OCV with increasing temperatures, indicating negative TC as illustrated in Fig. S15(a–d). The TC values are obtained by fitting the equilibrium state OCV against temperature, and the values are given in Table S2. The obtained TC values exhibit variation for different electrodes within the same electrolyte, suggesting that the entropy contributions from the electrode materials are likely to have a major impact on the isothermal reaction [68]. The negative TC values between −0.7 to −3 mV k^{-1} for all the systems are consistent with previous reports [69,70]. In ACC-based isothermal characterization, a TC of −0.73 mV K^{-1} was delivered because of the thermodiffusion of electrolyte ions [67]. In comparison to ACC, CS/ACC, NS/ACC, and NCS/ACC exhibited a higher TC due to their inherent redox characteristics, which facilitate enhanced electronic contribution or thermogalvanic effects [67]. The thermodiffusion contributions of CS/ACC, NS/ACC and NCS/ACC are 73, 34.4 and 24.3 %, respectively. And the thermogalavanic contributions of CS/ACC, NS/ACC and NCS/ACC are 27, 65.5 and 75.6 %, respectively. This isothermal analysis provides critical understanding of thermodiffusion and thermogalvanic contribution of selenide electrodes whose OCV changes for an increase in temperature. All these findings reveal that the redox type electrodes can exhibit ultrafast response to heat/electricity signals.

3.3.2. Non-isothermal characterization

Due to the enhanced electrochemical properties and comparatively higher TC value, the selenide electrodes are further extended to symmetric non-isothermal measurements in H-cell configuration as shown in Fig. 6(a). This study enables a better understanding of ion diffusion mechanisms involved in heat to current conversion. Two NCS/ACC electrodes are inserted into the two chambers of the H-Cell, each equipped with thermocouples to accurately measure the OCV (ΔV) and temperature. One chamber is placed on a hot plate while the other is placed on a cold-water bath to generate a temperature gradient (ΔT) between the two electrodes. A Celgard separator is interposed between the two chambers to prevent mixing of 1 M NaOH electrolyte and to facilitate ion transport. A temperature gradient ranging from 0 to 10 K

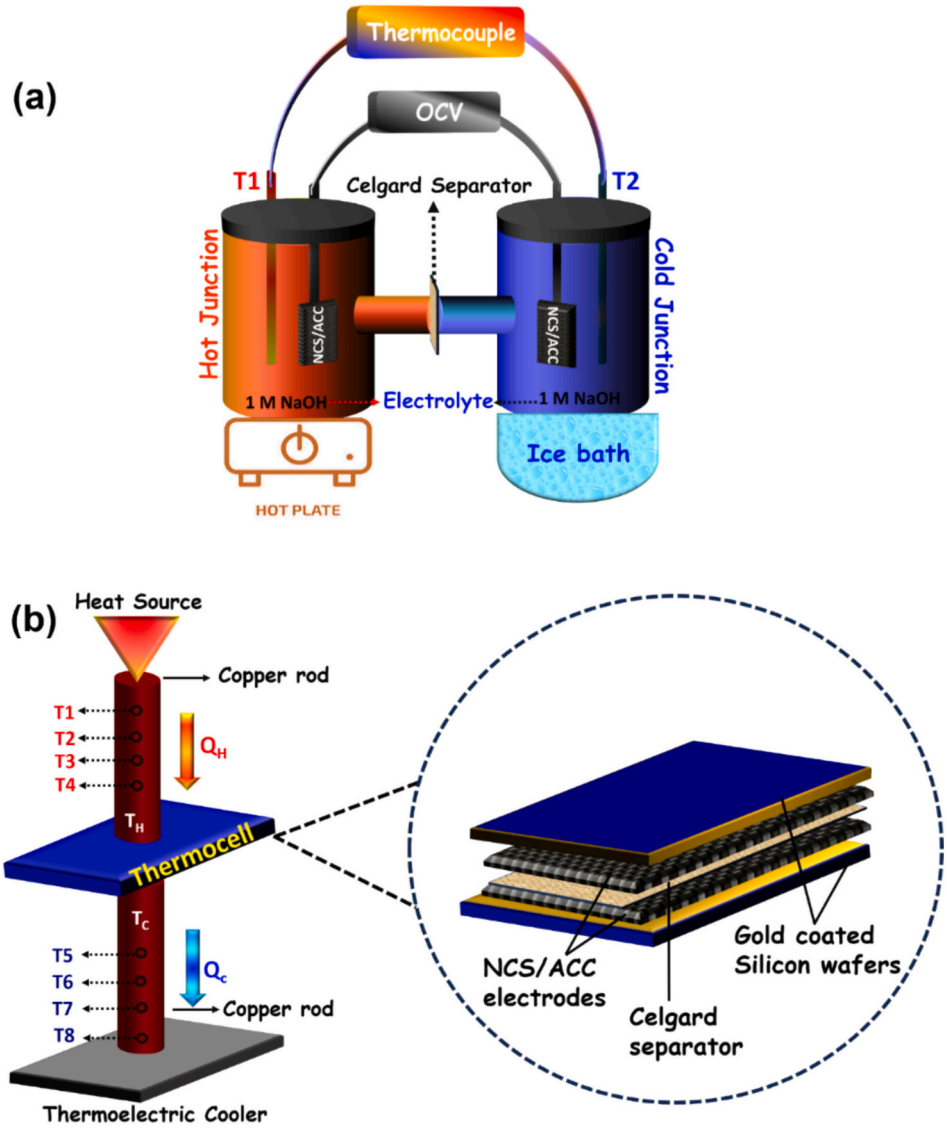


Fig. 6. Schematic representation of (a) H-type TEC and (b) sandwich type TEC.

was maintained between the hot and cold electrodes, and the resulting change in open circuit voltage (ΔV) of three different systems was subsequently recorded. Also, it can be observed that the ionic Seebeck effect has led to the movement of ions in response to a temperature gradient, resulting in the generation of a negative open circuit voltage as shown in Fig. 7(a–b). Once the temperature gradient is established between two electrodes, the balance of the reaction is broken, leading to oxidation at the hot side and reduction at the cold side [69]. In detail, the electrochemical redox reaction of the cold electrode can be described as follows: Ni^{3+}/Co^{3+} is reduced to Ni^{2+}/ Co^{2+}, while hydroxide ions (OH^-) are transferred to the hot electrode, where oxidation from Ni^{2+} to Ni^{3+} and Co^{2+} to Co^{3+} occurs. This leads to the generation of open circuit voltage in the TEC (Fig. S16) [71]. According to previous studies, it is significant to note that the thermal Soret effect is negligible in non-isothermal conditions, with values approximately 100 times smaller (around 10–50 μV/K). Thereby, the ionic Seebeck coefficient (S_e) can be calculated from the following equation [72]:

$$S_e = \frac{\Delta V}{\Delta T} \tag{12}$$

Also, the heat energy Q_{dis} associated with the chemical reaction in the TEC can be calculated using the following equation [72] :

$$Q_{dis} = T_H \Delta S \tag{13}$$

where T_H is the working temperature of TEC and ΔS is the entropy change, equals to the summation of entropy changes at positive and negative electrodes.

The OCV of CS/ACC electrode-based H-type cell deviated from near zero value, which is indeed not an ideal thermocell, as shown in Fig. S17. In an ideal thermocell, the OCV would be zero or close to zero, since there is no net current flow and no external driving force. Therefore, the Seebeck coefficient values can only be determined for NS/ACC, and NCS/ACC electrode-based H-type cells, which are −1.8 and −2 mV K^{-1}, respectively (as shown in Fig. 7(c and d)). Also, at the high temperature gradient, NS/ACC and NCS/ACC can store up to −0.54 and −0.6 J of heat energy, which is calculated from the Eq. (13). While $CoSe_2$ exhibits significant deviations from the ideal OCV behaviour, the addition of $NiSe_2$ layer in NCS/ACC mitigated these deviations and eventually improved the Seebeck coefficient and overall efficiency of the H-type cell. The synergistic effect of Ni and Co in NCS/ACC exhibits better thermal stability compared to their pure counterparts, enabling more reliable performance under varying temperature gradients, which is crucial for ionic thermoelectric applications. These S_e values of the fabricated selenide electrodes closely align with the TC values obtained

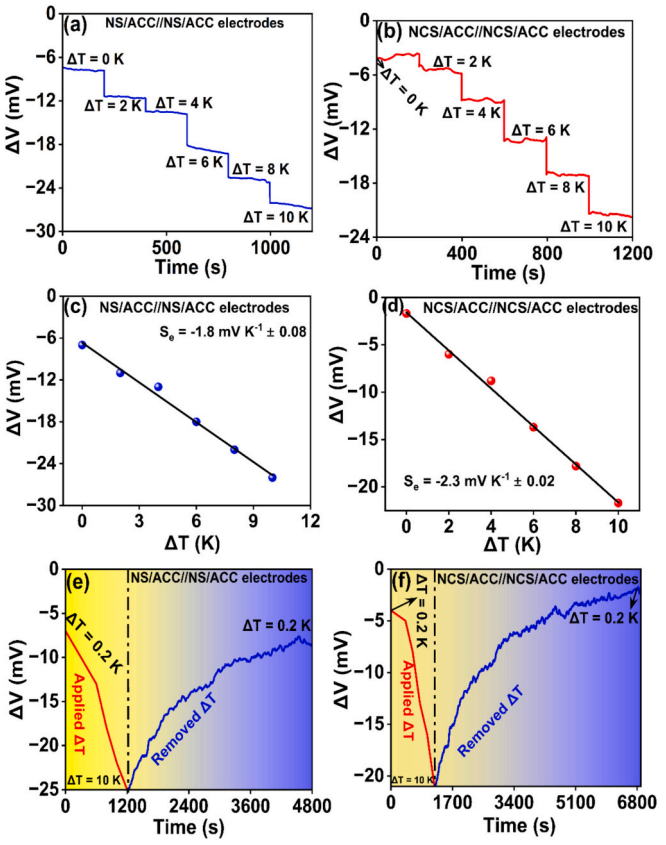


Fig. 7. H- type non-isothermal measurement of (a and b) OCV as a function of time under different temperature gradients (ΔT = 0 to 10 K), (c and d) Corresponding Seebeck voltage as a function of temperature gradients. (e and f) Effect on ΔV while applying and removing ΔT, for Symmetric H-type non-isothermal measurement based on NS/ACC and NCS/ACC electrodes, respectively.

from the isothermal configuration. This can be attributed to the selenide electrode's minimal entropy contribution when subjected to uniform temperature rise within the isothermal configuration. Subsequently, the temperature differences within the H-type cell can further lead to variations in ion distribution, ultimately resulting in a lower thermovoltage output. Other factors such as Ohmic resistance, activation and mass transport resistance can also minimise the thermovoltage [71]. Also, the previous reports suggested that the phase of the electrode material influences the entropy contribution and affects the overall thermovoltage of the system [72]. However, the NCS/ACC revealed a good Seebeck coefficient in aqueous 1 M NaOH electrolyte compared to other carbon-based electrodes in redox couple and ionic liquid electrolytes, as shown in Table S3.

From Table S3, it can be observed that carbon-based electrodes are highly preferred for heat-to-energy conversion applications because of their huge electrochemical surface area that leads to high current density under temperature gradient [73]. Also, redox couple electrolytes are mostly preferred because of their high entropy solvation and redox activity when subjected to temperature differences [74]. However, due to their toxicity in heating conditions, the current research focuses on employing sodium-based electrolytes for TEC. In this regard, the NCS/ACC-based symmetric H-type thermocell setup has revealed a promising thermovoltage of -2.3 mV K^{-1} in 1 M NaOH aqueous electrolyte. Further, Fig. 7(e–f) shows that when a temperature gradient is applied between the two electrodes, an increasing negative OCV occurs with time. Upon removal of the temperature gradient, the potential difference between the two electrodes decreases, leading to the restoration of the OCV to its initial value. The nanowire morphology and mesoporous nature (as explained in Brunauer–Emmett–Teller analysis shown in Fig. S6) of the NCS/ACC electrodes enhances charge transfer efficiency and reaction kinetics due to its high surface area and reduced diffusion pathways. This structure fosters rapid establishment and restoration of equilibrium within the thermo-electrochemical system, thereby validating the observed reversible open-circuit voltage behaviour.

The real-time heat-to-electricity conversion of selenide electrodes was evaluated using the modified ASTM D5470-06 based setup. A sandwich-type TEC was assembled with a 1 M NaOH infiltrated Celgard separator between two symmetric selenide electrodes. A thermal gradient was generated using copper bars, with one bar connected to a heat source and the other to a Peltier cooler as shown in Fig. 6(b). The heat flow was uniform and perpendicular to the surface of the thermocell, with minimum lateral heat spreading. Four thermistors are placed inside each copper bar to measure local temperatures, allowing for the extrapolation of the temperature at the contact surface of each bar with the thermocell. The working procedures of ASTM D5470-06 system is given in Reference [75].

The OCV of the TEC was measured as a function of temperature difference between hot and cold electrodes, as shown in Fig. 8(a and b). Fig. 8(c and d) showed that the OCV of the thermocell decreased linearly with increasing temperature difference, with slopes of -2.3 mV K^{-1} and -3.4 mV K^{-1} for NS/ACC and NCS/ACC based symmetric TEC, respectively. Compared to H-type electrochemical cells, the sandwich-type TEC exhibit a significantly shorter electrode-electrode distance, which enhances thermal diffusion and a substantial increase in thermovoltage. We also calculated the thermal charge storage based on Eq. (8), where the hot electrode temperature is at 30 °C. Here, the thermal charge storage increased from -0.69 and -1.02 J for NS/ACC and NCS/ACC based TECs, respectively. This is due to the reduced thermal

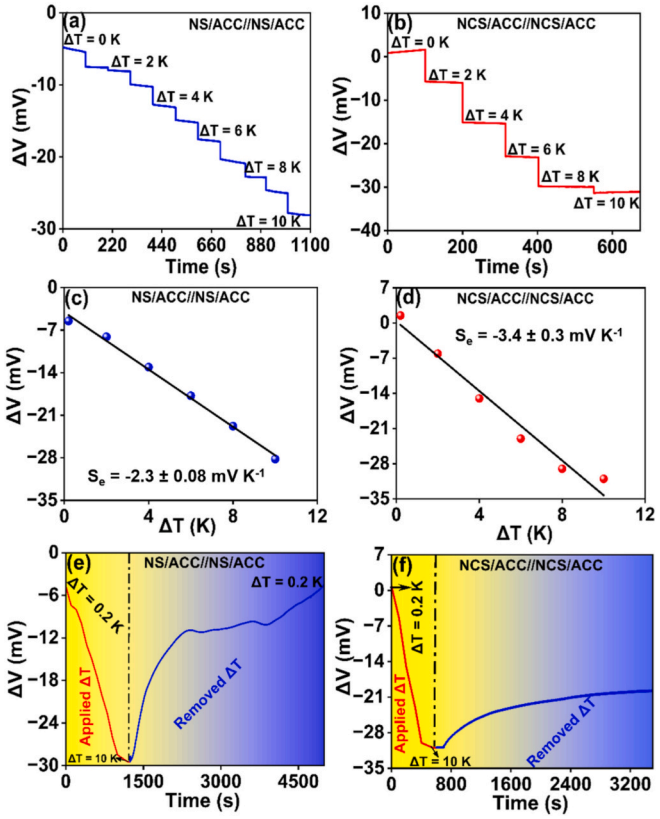


Fig. 8. Voltage (ΔV) as a function of time under different temperature gradients (ΔT = 0 to 10 K) for (a) NS/ACC and (b) NCS/ACC based TECs. (c and d) Corresponding Seebeck voltage as a function of temperature gradients. (e and f) Effect on ΔV while applying and removing ΔT, for NS/ACC and NCS/ACC electrodes, respectively.

resistance and increased thermal conductivity between the electrodes, allowing for more efficient heat transfer and thereby increasing the Seebeck coefficient and the resulting thermovoltage [76]. Additionally, Fig. 8(e and f) shows the reversible nature of the thermocell as demonstrated by restoring the OCV by removing the thermal gradient between the electrodes. Among all the fabricated selenide electrodes, NCS/ACC has revealed an excellent electrochemical performance and is the most promising candidate for charge storage and heat-to-electricity conversion application. This enhanced performance can be attributed to the unique crystal structure of the $NiSe_2$-$CoSe_2$ composite, which synergistically combines the advantageous properties of both components [24–27]. The variation in Fermi energies between $NiSe_2$ and $CoSe_2$ generates a built-in electric field that significantly facilitates the efficient transport of ions and electrons [24–27]. Additionally, the reduced dimensions of the nanowires, along with the conductive nature of the carbon support, further enhance the overall electrochemical performance [24–27]. Future research should explore the material composition and structure of NCS/ACC electrodes to enhance electrochemical charge storage and thermoelectric performance. Integrating NCS/ACC electrodes with other energy conversion technologies, such as hybrid systems, may lead to synergistic effects and improve overall efficiency for sustainable energy solutions.

4. Conclusions

In conclusion, the development of NCS-ACC electrodes represents a significant enhancement in harnessing dual functionality for thermal energy conversion and electrochemical charge storage. Impressively, a synergistic combination of $NiSe_2$-$CoSe_2$ nanowires on an ACC substrate not only enhances the electrochemical charge storage properties but also maximizes operational cyclic stability. With an excellent charge storage capacity of 112 mA h g^{-1} at a current density of 1 A g^{-1} and a remarkable cyclic stability of 85 % capacity retention over 10,000 cycles, the NCS-ACC electrodes are well-suited for advanced charge storage applications. Concurrently, their application in TEC, utilizing a 1 M NaOH aqueous electrolyte, has demonstrated significant thermoelectric performance, achieving a Seebeck coefficient of −3.4 mV K^{-1} and a thermal charge storage of −1.02 J under a thermal gradient of 10 K. This dual functionality not only enhances their potential as efficient charge storage materials but also showcases their capability for effective heat-to-electricity conversion. The NCS-ACC system thus emerges as a versatile candidate for innovative energy technologies, bridging the gap between electrochemical applications and thermal energy harvesting, ultimately paving the way towards integrated energy solutions.

CRediT authorship contribution statement

Rupa Ranjani Palanisamy: Writing – review & editing, Writing – original draft, Visualization, Validation, Methodology, Investigation, Formal analysis. **N. Padmanathan:** Writing – review & editing, Validation, Methodology, Investigation, Formal analysis, Conceptualization. **Anjali Ashokan:** Investigation, Formal analysis. **Amit Tanwar:** Methodology, Investigation. **Subhajit Biswas:** Writing – review & editing, Supervision, Methodology, Funding acquisition. **Justin D. Holmes:** Writing – review & editing, Supervision, Project administration, Funding acquisition. **Kafil M. Razeeb:** Writing – review & editing, Supervision, Resources, Project administration, Funding acquisition, Formal analysis, Data curation, Conceptualization.

Declaration of competing interest

The authors declare the following financial interests/personal relationships which may be considered as potential competing interests: Kafil M. Razeeb reports financial support was provided by Tyndall National Institute. If there are other authors, they declare that they have no known competing financial interests or personal relationships that could have appeared to influence the work reported in this paper.

Acknowledgements

Authors acknowledge the funding received from European Union's Horizon 2020 Research and Innovation Program under grant agreement number 96425 (TRANSLATE). This work also received support from Taighde Éireann – Research Ireland under Grant number 12/RC/2276. The carbon cloth activation and contact angle measurements was guided by Dr. Kamil Rahme, University College Cork. Initial discussion on the PAT-Core Cell analysis instrument with Prof. Colm O'Dwyer and Dr. Alex Grant from University College Cork is acknowledged.

Appendix A. Supplementary data

Supplementary data to this article can be found online at https://doi.org/10.1016/j.est.2025.116568.

Data availability

Data will be made available on request.

References

[1] Z. Dong, M. Chen, D. Qin, S. Han, Recent advances and perspective of modified TiO2-based photoanodes toward photoelectrochemical water splitting, Fuel 373 (2024), https://doi.org/10.1016/j.fuel.2024.132366.
[2] Z. Fu, Y. Zhu, D. Qin, Y. Yang, S. Han, Z. Dong, Functional coupling hole transport and extraction units over BiVO4 for efficient solar-to-hydrogen conversion, Energ. Conver. Manage. 322 (2024), https://doi.org/10.1016/j.enconman.2024.119153.
[3] Z. Dong, Q. Zhang, X. Shu, J. Hu, S. Han, Photo-assisted charging of heterostructured NiCo2S4@NiCo-LDH composite electrode with remarkable photoelectronic memory effect for high-performance asymmetric supercapacitor, Energ. Conver. Manage. 315 (2024), https://doi.org/10.1016/j.enconman.2024.118769.
[4] G. Tang, J. Liang, W. Wu, Transition metal selenides for supercapacitors, Adv. Funct. Mater. 34 (2024), https://doi.org/10.1002/adfm.202310399.
[5] K.K. Garlapati, A.R. Nath, A.M. Arjun, A. Vijayan, N. Sandhyarani, The rational investigation of bimetallic selenides as electrode materials for hybrid supercapacitors, Electrochim. Acta 424 (2022), https://doi.org/10.1016/j.electacta.2022.140627.
[6] Z. Fu, X. Shu, Q. Zhang, D. Qin, S. Han, Z. Dong, Solar-driven induced photoelectron remember effect involved in core–shell NiCo2S4@Ni3V2O8 composite electrode with superior electrochemical energy storage for asymmetric supercapacitor, Energ. Conver. Manage. 323 (2025), https://doi.org/10.1016/j.enconman.2024.119190.
[7] Y. Zhao, Q. Zhang, B. Sun, Y. Wang, X. Shu, Z. Dong, Recent progress of NiCo2S4-based electrodes materials for supercapacitor, J. Energy Storage 78 (2024), https://doi.org/10.1016/j.est.2023.109995.
[8] Y. Wang, F. Mo, X. Wu, Nickel-cobalt selenide nanosheets anchored on graphene for high performance all-solid-state asymmetric supercapacitors, J. Electroanal. Chem. 924 (2022), https://doi.org/10.1016/j.jelechem.2022.116863.
[9] K. Guo, S. Cui, H. Hou, W. Chen, L. Mi, Hierarchical ternary Ni-Co-Se nanowires for high-performance supercapacitor device design, Dalton Trans. 45 (2016) 19458–19465, https://doi.org/10.1039/C6DT03863H.
[10] P. Xu, W. Zeng, S. Luo, C. Ling, J. Xiao, A. Zhou, Y. Sun, K. Liao, 3D Ni-co selenide nanorod array grown on carbon fiber paper: towards high-performance flexible supercapacitor electrode with new energy storage mechanism, Electrochim. Acta 241 (2017) 41–49, https://doi.org/10.1016/j.electacta.2017.04.121.
[11] Q. Yang, Y. Liu, C. Deng, L. Sun, W. Shi, In-situ construction of heterostructure (Ni, co)Se2 nanoarrays derived from cone-like ZIF-L for high-performance hybrid supercapacitors, J. Colloid Interface Sci. 608 (2022) 3049–3058, https://doi.org/10.1016/j.jcis.2021.11.036.
[12] S. Li, W. Cai, X. Ma, J. Zhu, Y. Wang, Bimetallic cobalt-nickel selenide@polypyrrole core-shell nanotubes 011 nickel foam as high-performance electrode material for supercapacitors, Int. J. Electrochem. Sci. 15 (2020), https://doi.org/10.20964/2020.04.24.
[13] L. Wang, Z. Feng, H. Zhang, D. Li, P. Xing, One-step electrodeposited 3D porous NiCoSe2 nanosheet array for high-performance asymmetric supercapacitors, Nanotechnology 31 (2020), https://doi.org/10.1088/1361-6528/ab5bc2.
[14] L. Liu, Z. Li, W. Peng, J. Chang, H. Wang, Morphological modulation of NiCo2Se4 nanostructured arrays on carbon cloth and application to asymmetric supercapacitors, Solid State Ion. 386 (2022), https://doi.org/10.1016/j.ssi.2022.116046.
[15] Z.G. Chen, X. Shi, L.D. Zhao, J. Zou, High-performance SnSe thermoelectric materials: Progress and future challenge, Prog. Mater. Sci. 97 (2018) 283–346, https://doi.org/10.1016/j.pmatsci.2018.04.005.

[16] S. Zhang, S. Xiao, D. Li, J. Liao, F. Ji, H. Liu, L. Ci, Commercial carbon cloth: an emerging substrate for practical lithium metal batteries, Energy Storage Mater. 48 (2022) 172–190, https://doi.org/10.1016/j.ensm.2022.03.014.
[17] Y. Liu, M. Cui, W. Ling, L. Cheng, H. Lei, W. Li, Y. Huang, Thermo-electrochemical cells for heat to electricity conversion: from mechanisms, materials, strategies to applications, energy, Environ. Sci. 15 (2022) 3670–3687, https://doi.org/10.1039/d2ee01457b.
[18] I. Burmistrov, N. Kovyneva, N. Gorshkov, A. Gorokhovsky, A. Durakov, D. Artyukhov, N. Kiselev, Development of new electrode materials for thermo-electrochemical cells for waste heat harvesting, Renew. Energy Focus 29 (2019) 42–48, https://doi.org/10.1016/j.ref.2019.02.003.
[19] X. He, H. Sun, Z. Li, X. Chen, Z. Wang, Y. Niu, J. Jiang, C. Wang, Redox-induced thermocells for low-grade heat harvesting: mechanism, progress, and their applications, J. Mater. Chem. A Mater. 10 (2022) 20730–20755, https://doi.org/10.1039/d2ta05742e.
[20] T.J. Kang, S. Fang, M.E. Kozlov, C.S. Haines, N. Li, Y.H. Kim, Y. Chen, R. H. Baughman, Electrical power from nanotube and graphene electrochemical thermal energy harvesters, Adv. Funct. Mater. 22 (2012) 477–489, https://doi.org/10.1002/adfm.201101639.
[21] K. Kim, S. Hwang, H. Lee, Unravelling ionic speciation and hydration structure of Fe(III/II) redox couples for thermoelectrochemical cells, Electrochim. Acta 335 (2020), https://doi.org/10.1016/j.electacta.2020.135651.
[22] X. He, H. Sun, Z. Li, J. Song, H. Li, C. Wang, Y. Niu, J. Jiang, Simultaneously enhanced energy harvesting and storage performance achieved by 3D mix-phase Mose2-Nise/NF, Adv. Funct. Mater. 34 (2024), https://doi.org/10.1002/adfm.202307835.
[23] L. Shi, W. Yuan, J. Liu, W. Zhang, S. Hou, C. Hu, P-doped NiSe2 nanorods grown on activated carbon cloths for high-loading lithium-sulfur batteries, J. Alloys Compd. 875 (2021), https://doi.org/10.1016/j.jallcom.2021.160045.
[24] S. Maiti, A. Pramanik, S. Mahanty, Interconnected network of MnO2 nanowires with a “cocoonlike” morphology: redox couple-mediated performance enhancement in symmetric aqueous supercapacitor, ACS Appl. Mater. Interfaces 6 (2014) 10754–10762, https://doi.org/10.1021/am502638d.
[25] Z. Tian, Y. Liu, Q. Xu, Y. Shi, C. Ma, B. Peng, G. Liu, J. Yang, W. Zheng, Fe doped NiSe2 nanoarrays to boost electrocatalytic oxygen evolution reaction, Electrochim. Acta 425 (2022), https://doi.org/10.1016/j.electacta.2022.140711.
[26] H. Tabassum, C. Zhi, T. Hussain, T. Qiu, W. Aftab, R. Zou, Encapsulating Trogtalite CoSe2 Nanobuds into BCN nanotubes as high storage capacity sodium ion battery anodes, Adv. Energy Mater. 9 (2019), https://doi.org/10.1002/aenm.201901778.
[27] Q. Liu, Y. Ding, L. Zhang, Y. Li, C. Jiang, L. Cheng, Z. Li, Self-supported electrode constructed by hierarchical nickel-cobalt selenide nanosheet arrays for high-performance flexible supercapacitors, Colloids Surf. A Physicochem. Eng. Asp. 661 (2023), https://doi.org/10.1016/j.colsurfa.2023.130934.
[28] X. Xiao, L. Ni, G. Chen, G. Ai, J. Li, T. Qiu, X. Liu, Two-dimensional NiSe2 nanosheets on carbon fiber cloth for high-performance lithium-ion batteries, J. Alloys Compd. 821 (2020), https://doi.org/10.1016/j.jallcom.2019.153218.
[29] S. Tanwar, N. Singh, A.L. Sharma, Fabrication of activated carbon coated MSe2 (M=Mo, Co, and Ni) nanocomposite electrode for high-performance aqueous asymmetric supercapacitor, Colloids Surf. A Physicochem. Eng. Asp. 666 (2023), https://doi.org/10.1016/j.colsurfa.2023.131235.
[30] H. Yue, D. Yang, B. Yu, Y. Lu, W. Zhang, Y. Chen, Porous interwoven CoSe2/C microsphere: a highly efficient and stable nonprecious electrocatalyst for hydrogen evolution reaction, J. Mater. Sci. 54 (2019) 14123–14133, https://doi.org/10.1007/s10853-019-03881-2.
[31] D.P. Dutta, S. Abraham, Composite of α-FeOOH and mesoporous carbon derived from Indian blackberry seeds as low-cost and recyclable Photocatalyst for degradation of ciprofloxacin, Catalysts 13 (2023), https://doi.org/10.3390/catal13010191.
[32] D. Kong, J.J. Cha, H. Wang, H.R. Lee, Y. Cui, First-row transition metal dichalcogenide catalysts for hydrogen evolution reaction, energy, Environ. Sci. 6 (2013) 3553–3558, https://doi.org/10.1039/c3ee42413h.
[33] H. Zhou, Y. Wang, R. He, F. Yu, J. Sun, F. Wang, Y. Lan, Z. Ren, S. Chen, One-step synthesis of self-supported porous NiSe2/Ni hybrid foam: an efficient 3D electrode for hydrogen evolution reaction, Nano Energy 20 (2016) 29–36, https://doi.org/10.1016/j.nanoen.2015.12.008.
[34] H. Li, X. Qian, C. Zhu, X. Jiang, L. Shao, L. Hou, Template synthesis of CoSe2/Co3Se4 nanotubes: tuning of their crystal structures for photovoltaics and hydrogen evolution in alkaline medium, J. Mater. Chem. A Mater. 5 (2017) 4513–4526, https://doi.org/10.1039/c6ta10718d.
[35] H. Liu, Y. Lin, Y. Wu, L. Zhang, Y. Lu, M. Li, Preparation of NiSe2/CoSe2/C composites and their lithium storage properties, J. Mater. Sci. Mater. Electron. 32 (2021) 15059–15068, https://doi.org/10.1007/s10854-021-06058-3.
[36] X. Hu, X. Liu, K. Chen, G. Wang, H. Wang, Core-shell MOF-derived N-doped yolk-shell carbon nanocages homogenously filled with ZnSe and CoSe2 nanodots as excellent anode materials for lithium- and sodium-ion batteries, J. Mater. Chem. A Mater. 7 (2019) 11016–11037, https://doi.org/10.1039/c9ta01999e.
[37] S. Aftab, M.B. Tahir, M.S. Tahir, M. Sagir, Fabrication of NiCo2Se4@ NiWO4 nanocomposites for high performance supercapacitor applications, J. Energy Storage 56 (2022), https://doi.org/10.1016/j.est.2022.106111.
[38] C. Tang, L. Gan, R. Zhang, W. Lu, X. Jiang, A.M. Asiri, X. Sun, J. Wang, L. Chen, Ternary FexCo1-xP nanowire Array as a robust hydrogen evolution reaction Electrocatalyst with Pt-like activity: experimental and theoretical insight, Nano Lett. 16 (2016) 6617–6621, https://doi.org/10.1021/acs.nanolett.6b03332.
[39] B. Yu, X. Wang, F. Qi, B. Zheng, J. He, J. Lin, W. Zhang, Y. Li, Y. Chen, Self-assembled coral-like hierarchical architecture constructed by NiSe2 nanocrystals with comparable hydrogen-evolution performance of precious platinum catalyst, ACS Appl. Mater. Interfaces 9 (2017) 7154–7159, https://doi.org/10.1021/acsami.6b15719.
[40] B. Wang, X. Wang, B. Zheng, B. Yu, F. Qi, W. Zhang, Y. Li, Y. Chen, NiSe2 nanoparticles embedded in CNT networks: scalable synthesis and superior electrocatalytic activity for the hydrogen evolution reaction, Electrochem. Commun. 83 (2017) 51–55, https://doi.org/10.1016/j.elecom.2017.08.022.
[41] C. Xia, Q. Jiang, C. Zhao, M.N. Hedhili, H.N. Alshareef, Selenide-based Electrocatalysts and scaffolds for water oxidation applications, Adv. Mater. 28 (2016) 77–85, https://doi.org/10.1002/adma.201503906.
[42] J. Gao, Y. Li, L. Shi, J. Li, G. Zhang, Rational design of hierarchical nanotubes through encapsulating CoSe2 nanoparticles into MoSe2/C composite shells with enhanced lithium and sodium storage performance, ACS Appl. Mater. Interfaces 10 (2018) 20635–20642, https://doi.org/10.1021/acsami.8b06442.
[43] K. Okano, I. Saito, T. Mine, Y. Suzuki, T. Yamada, N. Rupesinghe, G.A. J. Amaratunga, W.I. Milne, D.R.T. Zahn, Characterizations of a-se based photodetectors using X-ray photoelectron spectroscopy and Raman spectroscopy, J. Non Cryst. Solids 353 (2007) 308–312, https://doi.org/10.1016/j.jnoncrysol.2006.11.007.
[44] Y. Gogotsi, R.M. Penner, Energy storage in nanomaterials - capacitive, Pseudocapacitive, or battery-like? ACS Nano 12 (2018) 2081–2083, https://doi.org/10.1021/acsnano.8b01914.
[45] S. Li, S. Wang, J. Wang, Optimal surface/diffusion-controlled kinetics of bimetallic selenide nanotubes for hybrid supercapacitors, J. Colloid Interface Sci. 617 (2022) 304–314, https://doi.org/10.1016/j.jcis.2022.02.125.
[46] C. Miao, X. Xiao, Y. Gong, K. Zhu, K. Cheng, K. Ye, J. Yan, D. Cao, G. Wang, P. Xu, Facile synthesis of metal-organic framework-derived CoSe2 nanoparticles embedded in the N-doped carbon Nanosheet Array and application for supercapacitors, ACS Appl. Mater. Interfaces 12 (2020) 9365–9375, https://doi.org/10.1021/acsami.9b22606.
[47] M. Pathak, D. Tamang, M. Kandasamy, B. Chakraborty, C.S. Rout, A comparative experimental and theoretical investigation on energy storage performance of CoSe2, NiSe2 and MnSe2 nanostructures, Appl. Mater. Today 19 (2020), https://doi.org/10.1016/j.apmt.2020.100568.
[48] J. Yang, Z. Sun, J. Wang, J. Zhang, Y. Qin, J. You, L. Xu, Hierarchical NiSe 2 spheres composed of tiny nanoparticles for high performance asymmetric supercapacitors, CrystEngComm 21 (2019) 994–1000, https://doi.org/10.1039/c8ce01805g.
[49] V. Subramanian, H. Zhu, R. Vajtai, P.M. Ajayan, B. Wei, Hydrothermal synthesis and pseudocapacitance properties of MnO 2 nanostructures, J. Phys. Chem. B 109 (2005) 20207–20214, https://doi.org/10.1021/jp0543330.
[50] M.W. Xu, D.D. Zhao, S.J. Bao, H.L. Li, Mesoporous amorphous MnO 2 as electrode material for supercapacitor, J. Solid State Electrochem. (2007) 1101–1107, https://doi.org/10.1007/s10008-006-0246-4.
[51] Y. Shao, M.F. El-Kady, J. Sun, Y. Li, Q. Zhang, M. Zhu, H. Wang, B. Dunn, R. B. Kaner, Design and mechanisms of asymmetric supercapacitors, Chem. Rev. 118 (2018) 9233–9280, https://doi.org/10.1021/acs.chemrev.8b00252.
[52] Y. Wang, Y. Song, Y. Xia, Electrochemical capacitors: mechanism, materials, systems, characterization and applications, Chem. Soc. Rev. 45 (2016) 5925–5950, https://doi.org/10.1039/c5cs00580a.
[53] X. Wang, G. Shen, Intercalation pseudo-capacitive TiNb2O7@carbon electrode for high-performance lithium ion hybrid electrochemical supercapacitors with ultrahigh energy density, Nano Energy 15 (2015) 104–115, https://doi.org/10.1016/j.nanoen.2015.04.011.
[54] J. Fu, L. Li, J.M. Yun, D. Lee, B.K. Ryu, K.H. Kim, Two-dimensional titanium carbide (MXene)-wrapped sisal-like NiCo2S4 as positive electrode for high-performance hybrid pouch-type asymmetric supercapacitor, Chem. Eng. J. 375 (2019), https://doi.org/10.1016/j.cej.2019.121939.
[55] K.S. Kim, N.M. Shinde, J.M. Yun, K.H. Kim, Sulfur and phosphorus co-doped nickel-cobalt layered double hydroxides for enhancing electrochemical reactivity and supercapacitor performance, RSC Adv. 11 (2021) 12449–12459, https://doi.org/10.1039/d1ra00424g.
[56] Y. Lan, H. Zhao, Y. Zong, X. Li, Y. Sun, J. Feng, Y. Wang, X. Zheng, Y. Du, Phosphorization boosts the capacitance of mixed metal nanosheet arrays for high performance supercapacitor electrodes, Nanoscale 10 (2018) 11775–11781, https://doi.org/10.1039/c8nr01229f.
[57] K.S. Bhat, S. Shenoy, H.S. Nagaraja, K. Sridharan, Porous cobalt chalcogenide nanostructures as high performance pseudo-capacitor electrodes, Electrochim. Acta 248 (2017) 188–196, https://doi.org/10.1016/j.electacta.2017.07.137.
[58] L.G. Beka, X. Li, W. Liu, Nickel cobalt sulfide core/shell structure on 3D graphene for supercapacitor application, Sci. Rep. 7 (2017), https://doi.org/10.1038/s41598-017-02309-8.
[59] R.N. Bulakhe, S.A. Arote, B. Kwon, S. Park, I. In, Facile synthesis of nickel cobalt sulfide nano flowers for high performance supercapacitor applications, Mater. Today Chem 15 (2020), https://doi.org/10.1016/j.mtchem.2019.100210.
[60] M. Xiao, S. Yang, M. Xiao, W. Zhang, X. Du, X. Hui, X. Niu, A new method for one-step hydrothermal synthesis of nickel cobalt selenide electrode material for supercapacitor, J. Mater. Sci. Mater. Electron. 34 (2023), https://doi.org/10.1007/s10854-023-10964-z.
[61] W. Raza, F. Ali, N. Raza, Y. Luo, K.H. Kim, J. Yang, S. Kumar, A. Mehmood, E. E. Kwon, Recent advancements in supercapacitor technology, Nano Energy 52 (2018) 441–473, https://doi.org/10.1016/j.nanoen.2018.08.013.
[62] Y. Meng, P. Sun, W. He, B. Teng, X. Xu, Uniform P doped co-Ni-S nanostructures for asymmetric supercapacitors with ultra-high energy densities, Nanoscale 11 (2019) 688–697, https://doi.org/10.1039/c8nr07454b.

[63] L.C. Qiu, Q.C. Wang, X.Y. Yue, Q.Q. Qiu, X.L. Li, D. Chen, X.J. Wu, Y.N. Zhou, NiCo2Se4 as an anode material for sodium-ion batteries, Electrochem. Commun. 112 (2020), https://doi.org/10.1016/j.elecom.2020.106684.
[64] Y.N. Zhou, M. Sina, N. Pereira, X. Yu, G.G. Amatucci, X.Q. Yang, F. Cosandey, K. W. Nam, Feo0.7F1.3/C nanocomposite as a high-capacity cathode material for sodium-ion batteries, Adv. Funct. Mater. 25 (2015) 696–703, https://doi.org/10.1002/adfm.201403241.
[65] P. Rupa Ranjani, P.M. Anjana, R.B. Rakhi, Solvothermal synthesis of CuFeS2 nanoflakes as a promising electrode material for supercapacitors, J. Energy Storage 33 (2021), https://doi.org/10.1016/j.est.2020.102063.
[66] X. Li, W. Yan, S. Guo, Y. Liu, J. Niu, L. Yin, Z. Wang, One-step electrochemical controllable preparation of nickel cobalt sulfide nanosheets and its application in supercapacitors, Electrochim. Acta 387 (2021), https://doi.org/10.1016/j.electacta.2021.138488.
[67] H. Wang, S.C. Kim, T. Rojas, Y. Zhu, Y. Li, L. Ma, K. Xu, A.T. Ngo, Y. Cui, Correlating Li-ion solvation structures and electrode potential temperature coefficients, J. Am. Chem. Soc. 143 (2021) 2264–2271, https://doi.org/10.1021/jacs.0c10587.
[68] Z. Li, Y. Xu, L. Wu, J. Cui, H. Dou, X. Zhang, Enabling giant thermopower by heterostructure engineering of hydrated vanadium pentoxide for zinc ion thermal charging cells, Nat. Commun. 14 (2023), https://doi.org/10.1038/s41467-023-42492-z.
[69] X. Wang, Y.T. Huang, C. Liu, K. Mu, K.H. Li, S. Wang, Y. Yang, L. Wang, C.H. Su, S. P. Feng, Direct thermal charging cell for converting low-grade heat to electricity, Nat. Commun. 10 (2019), https://doi.org/10.1038/s41467-019-12144-2.
[70] D. Artyukhov, N. Kiselev, E. Boychenko, A. Asmolova, D. Zheleznov, I. Artyukhov, I. Burmistrov, N. Gorshkov, High-power-density Thermoelectrochemical cell based on Ni/NiO nanostructured microsphere electrodes with alkaline electrolyte, Nanomaterials 13 (2023), https://doi.org/10.3390/nano13162290.
[71] M.A.M. Hasan, H. Wu, Y. Yang, Redox-induced electricity for energy scavenging and self-powered sensors, J. Mater. Chem. A Mater. 9 (2021) 19116–19148, https://doi.org/10.1039/d1ta02287c.
[72] J. Duan, B. Yu, L. Huang, B. Hu, M. Xu, G. Feng, J. Zhou, Liquid-state thermocells: opportunities and challenges for low-grade heat harvesting, Joule 5 (2021) 768–779, https://doi.org/10.1016/j.joule.2021.02.009.
[73] S. Zhang, Y. Zhou, Y. Liu, G.G. Wallace, S. Beirne, J. Chen, All-polymer wearable thermoelectrochemical cells harvesting body heat, IScience 24 (2021), https://doi.org/10.1016/j.isci.2021.103466.
[74] P.F. Salazar, S.T. Stephens, A.H. Kazim, J.M. Pringle, B.A. Cola, Enhanced thermo-electrochemical power using carbon nanotube additives in ionic liquid redox electrolytes, J. Mater. Chem. A Mater. 2 (2014) 20676–20682, https://doi.org/10.1039/c4ta04749d.
[75] A. Tanwar, S. Lal, R. Kaur, N. Padmanathan, E. Dalton, K.M. Razeeb, A fully automated measurement system for the characterization of micro thermoelectric devices near room temperature, Appl. Therm. Eng. 224 (2023), https://doi.org/10.1016/j.applthermaleng.2023.120111.
[76] Z. Mo, J. Zhou, X. Lu, L. Liang, F. Liu, Z. Liu, G. Chen, Flexible nanocomposite electrodes with optimized hybrid structure for improved low-grade heat harvest via thermocells, Sci. China Chem. 66 (2023) 1814–1823, https://doi.org/10.1007/s11426-023-1567-0.